MULTIFREQUENCY VERY LONG BASELINE ARRAY OBSERVATIONS OF THE COMPACT DOUBLE B2 2050+36: CONSTRAINTS ON INTERSTELLAR SCATTERING REVISITED

T. JOSEPH W. LAZIO

Remote Sensing Division, Code 7213, Naval Research Laboratory, 4555 Overlook Avenue, SW, Washington, DC 20375-5351; lazio@rsd.nrl.navy.mil

AND

A. L. FEY

US Naval Observatory, 3450 Massachusetts Avenue NW, Washington, DC 20392-5420; afey@usno.navy.mil

ABSTRACT

We present multifrequency observations with the Very Long Baseline Array of the compact double radio source B2 2050+36. Our observations are at 0.33, 0.61, 1.67, 2.3, and 8.4 GHz, with the 0.61 GHz observations forming the third epoch of observation of this source at that frequency. At 0.61 GHz, the structure of B2 2050+36 is dominated by two components 56 mas apart. Within the uncertainties of the various measurements, this separation has remained unchanged for the past 16 yr. Any differential image wander caused by refractive interstellar scattering is less than 4 mas. Both the lack of differential image wander and the frequency dependence of the angular diameter of B2 2050+36 below 1 GHz indicate that the electron density power spectrum along this line of sight has a spectral index near the Kolmogorov value, with a value of 4 being highly unlikely. We conclude that diffractive scattering dominates along this line of sight; results in the literature indicate that this conclusion also holds true for the line of sight to the pulsar PSR B2020+28 (8°.7 from B2 2050+36). Comparison of our 1.67 GHz observations with those obtained 21 yr previously place a limit on the projected linear separation velocity of the two components of c.

Subject headings: galaxies: active — galaxies: individual (B2 2050+36) — ISM: structure — radio continuum: ISM — scattering — turbulence

1. INTRODUCTION

Density fluctuations on AU-size scales in the interstellar plasma may produce a host of observable effects including refractive intensity scintillations and image wander. The magnitude of these effects depends crucially on the spectrum of the interstellar density fluctuations. If the spectrum is a power law with a spectral index less than 4, these refractive effects will generally be masked by diffractive effects from even smaller scale density fluctuations (Romani, Narayan, & Blanford 1986). Conversely, if the spectrum is a power law with a spectral index greater than 4, refractive effects will dominate. For many lines of sight, the density spectral index appears to be close to, but less than, 4 (Armstrong, Rickett, & Spangler 1995), with important exceptions (see, e.g., Hewish, Wolszczan, & Graham 1985; Clegg, Fiedler, & Cordes 1993; Gupta, Rickett, & Lyne 1994; Stinebring, Faison, & McKinnon 1996; Rickett, Lyne, & Gupta 1997).

Complicating the effort to measure refractive effects is their generally long timescale. The relevant timescale is given by the time it takes for an AU-sized density fluctuation to drift past the observer. For observations of pulsars, whose velocities can exceed 100 km s^{-1}, the timescale is days. For observations of extragalactic sources, the relevant velocity is a combination of the Earth's velocity and random interstellar motions and is more likely to be roughly 25 km s^{-1}, meaning that the refractive timescale is months to years.

The source B2 2050+36 is an ideal source for probing refractive effects. It lies on the outskirts of the Cygnus superbubble (Bochkarev & Sitnik 1985), a region known to exhibit enhanced interstellar scattering (Fey, Spangler, & Mutel 1989; Lazio, Spangler, & Cordes 1990; Fey, Span-

gler, & Cordes 1991; Wilkinson, Narayan, & Spencer 1994; Molnar et al. 1995; Spangler & Cordes 1998). VLBI observations reveal its milliarcsecond structure to be dominated by two components separated by approximately 60 mas; thus, a search for refractive image wander requires only *relative* position measurements.

Fey & Mutel (1993, hereafter FM93) obtained 0.61 GHz VLBI observations of B2 2050+36. Combined with previous measurements in the literature, they showed that scattering is moderately strong along this line of sight. They were also able to constrain the amount of differential refractive image wander between the two components. Their constraint, however, is based on measurements of the separation of the components at two epochs separated by 4 yr. If the refractive timescale is longer than 4 yr, their constraint is weakened considerably. Assuming that typical interstellar velocities along this line of sight are 50–100 km s^{-1}, FM93 argued that the refractive timescale is comparable to or less than 4 yr. Obviously, if the typical interstellar velocity is more like 25 km s^{-1}, the refractive timescale is much longer.

We have acquired a third epoch of 0.61 GHz VLBI observations of B2 2050+36, specifically to confront the conclusions of FM93 with another epoch of observations. This third epoch is 12–16 yr after the first two epochs and should allow us to place much better constraints on any refractive wander. We have also acquired simultaneous or quasi-simultaneous observations at a range of other wavelengths in order to confirm previous measurements of the strength of interstellar scattering along this line of sight.

In § 2 we describe our observations and data analysis, in § 3 we discuss the implications of our observations for both diffractive and refractive interstellar scattering along this

TABLE 1

VLBA OBSERVING LOG

Frequency (GHz)	Bandwidth (MHz)	Recorded Polarization	On-source Time (hr)	Synthesized Beam (mas)	Image Noise Level[a] (mJy beam^{-1})
0.33	12	R, L	2.88[b]	61 × 58 at 87°	3.2
0.61	4	R, L	2.88[b]	27 × 19 at 14°	5
1.67	32	R, L	2.93	7.3 × 4.7 at −7°9	0.78
2.27	16	R, L	2.92[c]	5.8 × 3.6 at −9°4	1.1
8.42	16	R, L	2.92[c]	1.9 × 1.4 at −10°	0.61

[a] All images are of Stokes I polarization.
[b] Observations at 0.33 and 0.61 GHz were conducted simultaneously.
[c] Observations at 2.27 and 8.42 GHz were conducted simultaneously.

line of sight, and in § 4 we discuss the limits our observations place on the intrinsic structure and kinematics of the source. We present our conclusions in § 5.

2. OBSERVATIONS AND DATA ANALYSIS

We observed B2 2050+36 with the Very Long Baseline Array (VLBA) for a total of 10 hr on 2000 July 25. Relevant observation parameters are summarized in Table 1.

The observation frequencies were 0.33, 0.61, 1.67, 2.3, and 8.4 GHz; both right and left circular polarizations were recorded at all frequencies. The 2.3 and 8.4 GHz observations were obtained simultaneously in "S/X mode." Simultaneous 0.33 and 0.61 GHz observations also were obtained by setting two of the eight baseband converters (BBCs) at each VLBA antenna to record the two senses of circular polarization at 0.61 GHz. Because of severe radio

TABLE 2

GAUSSIAN SOURCE MODELS

v (GHz)	S (Jy)	r (mas)	θ (deg)	a (mas)	b/a	ϕ (deg)	Component
0.33....	2.17	0.0	...	106.2	0.76	−35	E[a]
0.61....	2.48	0.0	...	24.1	0.82	24	E
	0.39	56.1	−82	26.2	0.69	8	W
	0.11	32.6	8	47.5	0.00	67	E
1.67....	1.75	59.3	−80	3.5	0.90	−49	W
	0.79	5.5	−82	4.2	0.74	−19	E
	0.99	1.3	−132	4.0	0.86	33	E
	1.06	3.4	42	4.9	0.69	−77	E
	0.16	8.9	−106	11.8	0.32	−52	E
2.27....	1.97	0.0	−32	2.9	0.71	−61	W
	0.92	58.5	101	3.7	0.81	17	E
	0.58	53.8	100	3.3	0.59	−25	E
	0.83	61.5	97	4.2	0.54	−78	E
	0.12	52.9	103	7.5	0.39	−46	E
8.42....	0.35	18.4	−89	0.8	0.54	84	W
	0.39	20.1	−87	1.0	0.51	−1	W
	0.19	34.9	103	2.1	0.64	−29	E
	0.19	40.3	105	2.1	0.54	60	E
	0.19	43.2	99	3.5	0.51	−85	E
	0.22	18.8	−85	3.1	0.24	−67	W
	0.16	39.0	102.4	6.3	0.28	40	E

NOTE.—The models fitted to the visibility data are Gaussians with flux density S and FWHM major axis a and minor axis b, with major axis in position angle ϕ (measured north through east). Components are separated from the (arbitrary) origin of the image by a distance r in position angle θ, which is the position angle (measured north through east) of a line joining the components with the origin. Components and subcomponents are identified as with either an "E" or "W" corresponding to whether they are eastern or western, respectively.
[a] Assumed eastern component; see § 3.1.

frequency interference around 0.61 GHz, filters restricted the observable bandwidth for each BBC to 4 MHz. The remaining BBCs recorded at 0.33 GHz. Formatter problems at the Kitt Peak antenna meant that only nine of the 10 VLBA antennas were correlated.

The correlated visibilities were processed in the standard fashion within the NRAO AIPS. Fringe-fitting intervals ranged from 10 minutes at 1.67 GHz to 3 minutes at 0.33 and 8.4 GHz. At 0.33 and 0.61 GHz, substantial editing of the calibrated visibilities was required to remove radio frequency interference (RFI).

In general, the calibrated visibilities were then exported to the Caltech DIFMAP program for hybrid mapping. To ensure a robust estimate for the separation of the components (§ 3.2), the 0.61 GHz observations were imaged using both AIPS and DIFMAP; the 0.33 GHz observations were imaged using only AIPS.

Figure 1 shows the images of B2 2050+36 at the various frequencies. The observed rms noise level in these images ranges from 0.61 mJy beam^{-1} at 8.42 GHz to 5 mJy beam^{-1} at 0.61 GHz and is summarized in Table 1. The rms noise levels in our images are roughly within a factor of 2–3 of the expected value.

Using the images shown in Figure 1 as a guide, we fitted the self-calibrated visibility data with multiple Gaussian component models. The number of Gaussian components fitted ranged from 1 at 0.33 GHz to 7 at 8.42 GHz. These models are summarized in Table 2. Below we shall make use of the fitted angular diameters. At the higher frequencies, we take the uncertainty in a fitted angular diameter to be one-half of the synthesized beam; at the lower frequencies, where a one- or two-component fit suffices, we take the uncertainties to be the square roots of the diagonal elements of the covariance matrix obtained from a least-squares fit to the visibility data (provided by the UVFIT fitting routine within AIPS); these values are on the order of 0.5 mas.

3. CONSTRAINTS ON INTERSTELLAR SCATTERING

We now revisit the scattering properties of the line of sight to B2 2050+36. We consider both diffractive effects (namely, angular broadening) and refractive effects (namely, differential image wander and refractive intensity fluctuations).

We shall make the standard assumption throughout that the density fluctuations responsible for interstellar scattering can be parameterized by an exponentially truncated power law

$$P_{\delta n_e}(z, q) = C_n^2(z) q^{-\alpha} e^{-(q/q_1)^2}, \quad q > q_0. \quad (1)$$
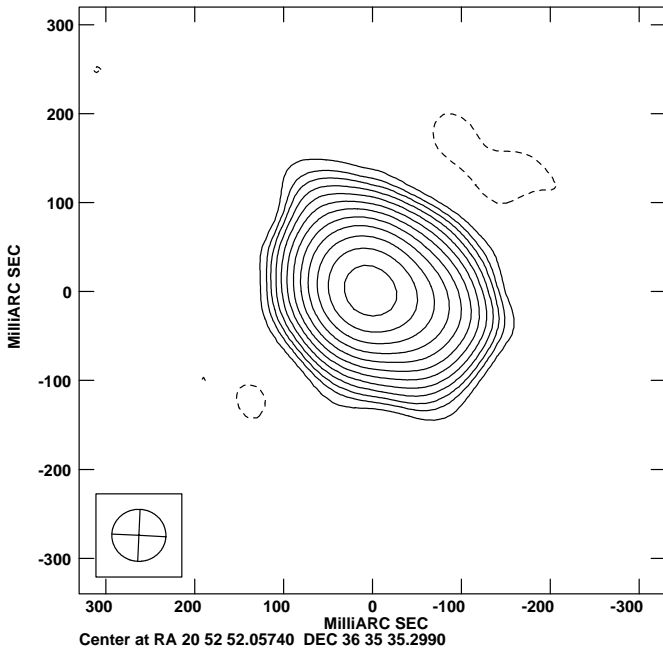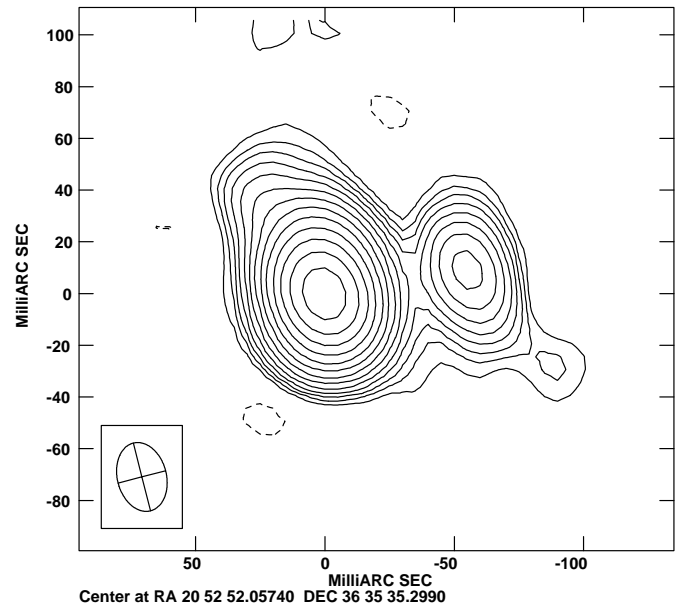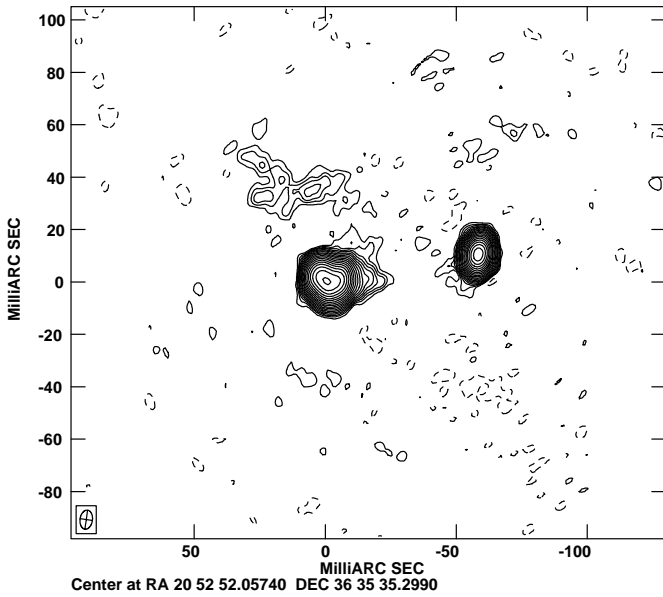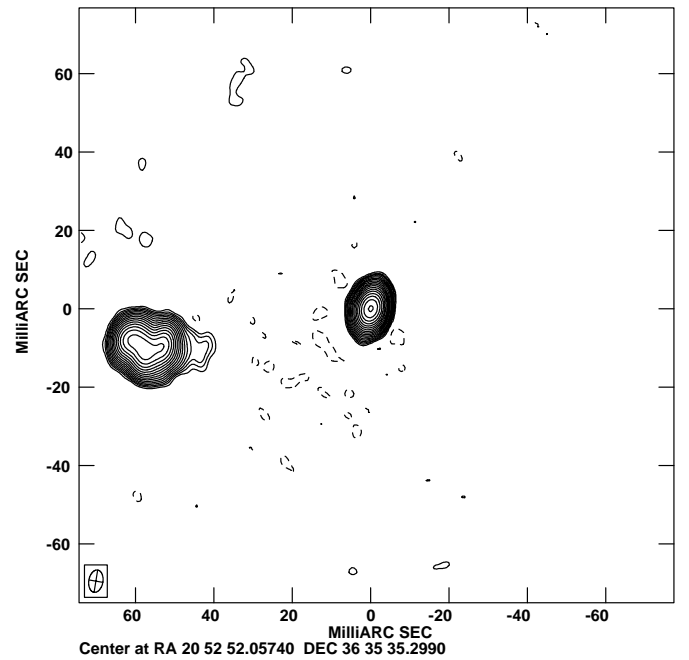
Fig. 1a

Fig. 1b

Fig. 1c

Fig. 1d

FIG. 1.—VLBI images of B2 2050 + 36. (a) 0.33 GHz. The rms noise level is 3.2 mJy beam^{-1}, and the contour levels are $(3.2 \times -2, 3, 5, 7.1, 10 \ldots)$ mJy beam^{-1}. The beam is 60.8×58.5 mas at a position angle of $87°$ and is shown in the lower left-hand corner. (b) 0.61 GHz. The rms noise level is 5 mJy beam^{-1}, and the contour levels are $(5 \times -3, 3, 5, 7.1, 10 \ldots)$ mJy beam^{-1}. The beam is 27×19 mas at a position angle of $14°$ and is shown in the lower left-hand corner. (c) 1.67 GHz. The rms noise level is 0.78 mJy beam^{-1}, and the contour levels are $(0.78 \times -3, 3, 5, 7.1, 10 \ldots)$ mJy beam^{-1}. The beam is 7.3×4.7 mas at a position angle of $-7°9$ and is shown in the lower left-hand corner. (d) 2.3 GHz. The rms noise level is 1.1 mJy beam^{-1}, and the contour levels are $(1.1 \times -3, 3, 5, 7.1, 10 \ldots)$ mJy beam^{-1}. The beam is 5.8×3.6 mas at a position angle of $-9°4$ and is shown in the lower left-hand corner. (e) 8.4 GHz. The rms noise level is 0.61 mJy beam^{-1}, and the contour levels are $(0.61 \times -3, 3, 5, 7.1, 10 \ldots)$ mJy beam^{-1}. The beam is 1.9×1.4 mas at a position angle of $-10°$ and is shown in the lower left-hand corner.

Here q_1 is the largest wavenumber on which density fluctuations occur, which is related to the smallest length scales for density fluctuations l_1, or the "inner scale," as $q_1 = 2\pi/l_1$. The smallest wavenumber on which density fluctuations occur, or the "outer scale," is $q_0 = 2\pi/l_0$. The constant C_n^2 is a measure of the level of density fluctuations and is related to the rms density as $\langle n_e^2 \rangle = [2(2\pi)^{4-\alpha}/(\alpha - 3)]C_n^2 l_0^{3-\alpha}$ (Cordes et al. 1991). The power-law spectral index is assumed to provide clues about the process(es) that generate or maintain the density fluctuations. Our observations allow us to measure α, constrain C_n^2, and indirectly place limits on l_1.

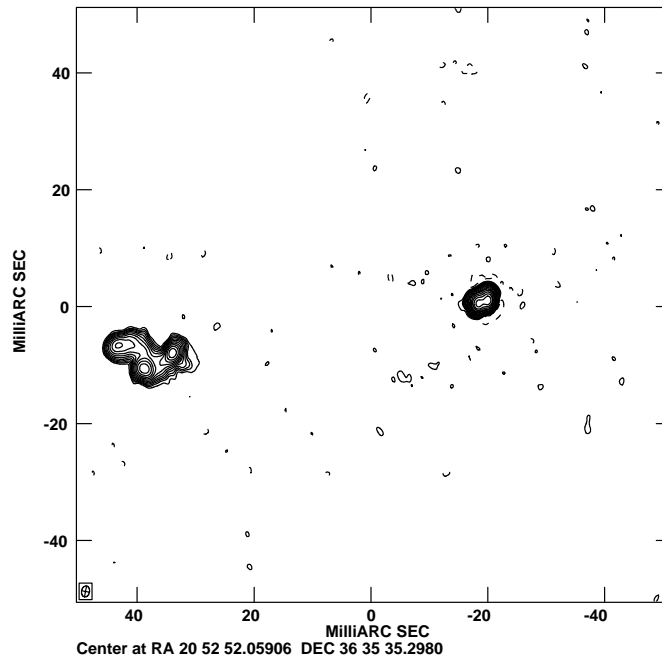Center at RA 20 52 52.05906 DEC 36 35 35.2980

FIG. 1e

3.1. Diffractive Scattering

3.1.1. Angular Broadening and Density Spectrum

An infinitely distant point source viewed through a medium filled with density fluctuations having a spectrum described by equation (1) and a spectral index $\alpha = 11/3$ will be broadened to an angular diameter (Cordes & Lazio 1991; Taylor & Cordes 1993)

$$\theta_d = \begin{cases} 128 \text{ mas } SM^{3/5} \nu_{GHz}^{-11/5}, & \theta_d \lesssim \theta_{cross}, \\ 132 \text{ mas } SM^{1/2} \nu_{GHz}^{-2} \left(\dfrac{l_1}{100 \text{ km}}\right)^{-1/6}, & \theta_d \gtrsim \theta_{cross}. \end{cases}$$

(2)

Here ν_{GHz} is the observing frequency measured in GHz and the scattering measure SM is the line of sight integral of C_n^2,

$$SM = \int dz \, C_n^2(z) .$$

(3)

The quantity θ_{cross} is the crossover angle and describes the relative importance of the inner scale l_1. It is given by $\theta_{cross} \simeq 0''.16\nu_{GHz}^{-1}(l_1/100 \text{ km})^{-1}$. The constants (128 and 132 mas) given in equation (2) are those appropriate for infinitely distant sources and differ slightly from those given by Cordes & Lazio (1991), who considered sources embedded in the medium. These formulae specify the diameter as FWHM of the shape of the image, and that will be the convention we adopt in reporting the measured diameters.

The scattering diameter θ_d defines the diffractive scale $l_d = \lambda/\theta_d$ (at observing wavelength λ). If the typical interferometer baseline b is sufficient to resolve θ_d (i.e., $b \sim l_d$) and $b \lesssim l_1$, we expect $\theta_d \gtrsim \theta_{cross}$ and $\theta_d \propto \nu^{-2}$. Conversely if $b \gtrsim l_1$, then we expect $\theta_d \lesssim \theta_{cross}$ and $\theta_d \propto \nu^{-11/5}$. Therefore, fitting the observed diameter as a function of frequency can constrain both l_1 and α.

There are alternate causes for a $\theta_d \propto \nu^{-2}$ dependence. For instance, if the spectrum of density fluctuations is not a power law but a Gaussian centered on a particular length scale, that can produce a $\theta_d \propto \nu^{-2}$ dependence. Similarly, if the density spectrum is dominated just slightly by AU-size scales such that $\alpha \gtrsim 4$, that could also produce an apparent $\theta_d \propto \nu^{-2}$ dependence within the measurement uncertainties. As we shall show below, $\alpha < 4$ so that we could interpret a $\theta_d \propto \nu^{-2}$ dependence as resulting from a "large" inner scale.

Figure 2 shows the measured angular diameters as a function of observing frequency. Also shown are two curves, one for $\theta \propto \nu^{-2.2}$ appropriate for a spectrum with $\alpha = 11/3$ and a diffractive scale l_d much larger than l_1 and one for $\theta \propto \nu^{-2}$ appropriate for the case in which $l_d \lesssim l_1$.

As Figure 1 demonstrates, B2 2050+36 is not only not a point source, but the two components of it can be resolved into multiple subcomponents at high frequencies. A visual inspection of Figure 2 suggests that at frequencies below 1 GHz, scattering dominates the structure of B2 2050+36, while at frequencies above 1 GHz, there are clear deviations from either curve presumably due to intrinsic structure. In order to quantify this result, we have fitted the measured diameters of the eastern component (Table 2) with the following functional form:

$$\theta^2 = \theta_i^2 + \theta_s^2 \, \nu_{GHz}^{-2\alpha/(\alpha-2)} .$$

(4)

Here θ_i is the intrinsic diameter and θ_s is the scattering diameter, both at the fiducial frequency of 1 GHz. Unlike in equation (2), in which we specified the dependence for the specific case of $\alpha = 11/3$, here we allow the frequency dependence to be part of the fit. The frequency dependence we use is appropriate for $\alpha < 4$.

Several points are in order regarding the choice of data we used. At 0.33 GHz, only one component is seen (Fig. 1a). Attempts to fit the visibility data with a two-component structure suggested by the 0.61 GHz image produced a poorer fit to the data. We have subtracted a one-component model (Table 2) from the visibility data and imaged the residuals. There is no indication of a second component at the location expected from the higher frequency images. We
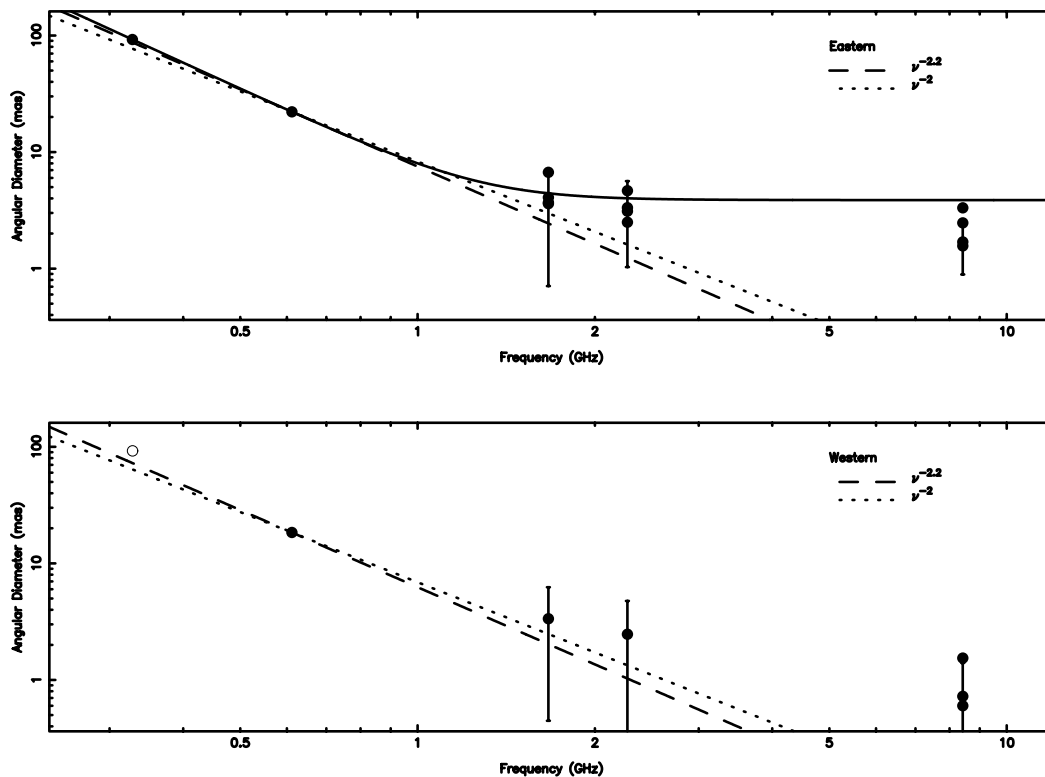
Fig. 2.—Angular diameter of the components of B2 2050 + 36 as a function of observing frequency. All components listed in Table 2 are plotted. *Top panel*: The eastern component. *Bottom panel*: The western component. For the western component, we also show, as an open circle, the diameter it would have assuming if its scattering diameter were identical to that of the eastern component. This point is shown for display purposes only and is not used in any of the fits described. In both panels a dashed line shows the dependence $\theta \propto \nu^{-2.2}$, as expected for a Kolmogorov spectrum, and a dotted line shows $\theta \propto \nu^{-2}$. Both lines are normalized to pass through the measured angular diameter at 0.61 GHz. For the eastern component only, a solid line shows the fit, which allows for intrinsic structure and which is discussed in the text. At the higher frequencies, we plot all subcomponents, but we show the uncertainty on only one of them since we assume the uncertainty to be the same for all subcomponents and equal to one-half of the synthesized beam.

have also produced model visibility data, comprised of two components whose flux densities, diameters, and positions are consistent with those seen at higher frequencies. Fitting these model data with a one-component model results in a fit nearly the same as what we find by fitting the observed visibility data. The similarity suggests that any systematic error in determining the diameter is probably no more than 1 mas. Because of the self-calibration we performed, we have no absolute position information. Given that the eastern component is stronger at 0.61 GHz, we have therefore assumed that the single component seen at 0.33 GHz is the eastern component.

At the higher frequencies, both components can be resolved into multiple subcomponents. In Figure 2 we plot the diameters of the individual subcomponents. The diameters of the individual subcomponents are clearly not representative of the diameter of the entire component. Therefore, as a measure of the size of the components at these frequencies, we have added the diameters of the subcomponents (Table 2) in quadrature. If anything, this estimate will *underestimate* the size of a component. However, our primary interest is not in the intrinsic structure, and this procedure suffices to obtain an estimate for the intrinsic size.

B2 2050 + 36 is classified as a gigahertz-peaked spectrum source, and both components show a single flux density maximum near 1 GHz (Mutel, Hodges, & Phillips 1985). Accordingly, in equation (4) we have assumed that the intrinsic structure has no frequency dependence. While we

have not conducted extensive tests, assuming no frequency dependence produces clearly much better fits than does assuming a frequency dependence of ν^{-1}, as might be expected for a homogeneous source with a peak brightness temperature T_B (Kellermann & Owen 1988).

We have used a grid-search technique to minimize the difference, in a χ^2 sense, between the data and the expression of equation (4) for the three parameters: θ_i, θ_s, and α. We have also determined the allowed ranges for the parameters in the following manner: holding two parameters fixed at the values that minimize χ^2, we change the third parameter until χ^2 changes by unity.

Table 3 summarizes the best-fit value for the parameters and their allowed ranges. The best-fitting curve is also shown in Figure 2. A key result of this fit is that a density

TABLE 3

BEST-FIT DIFFRACTIVE SCATTERING MODEL PARAMETERS
FOR EASTERN COMPONENT AT 1 GHz

Parameter	Adopted Value	Range
θ_i (mas)	3.9	3.5–4.3
θ_s (mas)	7.0	6.98–7.03
α	3.52	3.51–3.53
Derived Scattering Parameters		
SM[a] (kpc m$^{-20/3}$)	$10^{-2.1}$	
l_1 (km)	$\ll 2000$	

[a] Kolmogorov density spectrum, $\alpha = 11/3$, assumed.

spectrum spectral index of 4 is highly unlikely. This result means that the inner scale l_1 is substantially smaller than most baselines in the array or that $\theta_d < \theta_{cross}$. The typical array baseline is roughly 2000 km, so we place an upper limit of $l_1 \ll 2000$ km. This constraint is not a serious challenge to the value estimated by Spangler & Gwinn (1990) of $l_1 \lesssim 200$ km. Using equation (2), we can also derive the scattering measure SM. Table 3 also lists the values of these derived quantities.

3.1.2. *Image Anisotropy and Orientation*

The anisotropy and orientation of a scattered image can, in principle, yield information about the density structures responsible for the angular broadening (see, e.g., Wilkinson et al. 1994; Trotter, Moran, & Rodríguez 1998; Cordes & Lazio 2001). The simultaneous low-frequency observations we report here are seemingly ideal for constraining any wavelength-dependent changes in the anisotropy or orientation of B2 2050+36 since the u-v plane coverage should be identical (once scaled by the ratio of the wavelengths).

We consider first the anisotropy of the image. We find axial ratios of $b/a \simeq 0.80$ (Table 2) or, in terms of the image anisotropy parameter of Romani et al. (1986), $e_s \simeq 0.25$. Romani et al. (1986) also provide an estimate of the image anisotropy to be expected from random fluctuations within the medium. For our observing wavelengths and scattering parameters derived above, the expected random contribution to e_s is approximately 0.03. We conclude that these image anisotropies are significant. These anisotropies are also comparable to those of other sources seen through the Cygnus region (Spangler & Cordes 1988, 1998; Wilkinson et al. 1994; Molnar et al. 1995; Desai & Fey 2001). Desai & Fey (2001) attribute the similarity of the axial ratios between different sources at different frequencies and different epochs to be indicative of an anisotropy in the scattering material itself.

We cannot conclude that the image anisotropy changes with frequency for B2 2050+36. The formal uncertainties from the fitting of the visibility data are approximately 1%. Even this small uncertainty on the angular diameters, when propagated to the axial ratios, implies an uncertainty of $\Delta(b/a) \simeq 0.03$, comparable to the difference between the axial ratios at the two frequencies (Table 2).

Changes in the image orientation between the two frequencies may reflect changes in the orientation of the density irregularities responsible for the scattering. Unfortunately, we also cannot draw any conclusions about the image orientation. Although the u-v plane coverage should be similar, differences in the editing (due to the significant levels of RFI encountered) change the relative u-v plane coverage significantly. An indication of the difference can be seen by inspecting the synthesized beams shown in Figures 1a and 1b. In particular, the synthesized beam at 610 MHz has an orientation of 14° compared to an orientation for the eastern component of 24°. Thus, the apparent change in orientation between 330 ($-35°$) and 610 MHz (24°) may be largely due to the differences in u-v coverage.

3.2. *Refractive Interstellar Scattering*

Large-scale density fluctuations may affect the image position and flux density. In this section we place constraints on the strength of refractive modulation of the image, focusing primarily on the 0.61 MHz image.

3.2.1. *Differential Image Wander*

Density fluctuations on a scale $l_r = D\theta_d$, where D is the characteristic distance to the scattering medium, will cause refractive "bending" and "steering" of the propagating rays. In turn, this will affect the angle of arrival of rays and make radio sources wander about a true or nominal position. The magnitude of this effect depends both on the strength of scattering and the value of α.

FM93 selected B2 2050+36 because its two-component structure allowed for *relative* position measurements to be performed, obviating the need for determining absolute positions with milliarcsecond accuracy. FM93 summarized the predictions for the amount of differential angular wander as a function of α as predicted by various groups (Cordes, Pidwerbedsky, & Lovelace 1986; Romani et al. 1986; Rickett & Coles 1988; see Appendix A of FM93). They found that the rms differential refractive angular wander is

$$\langle \Delta\theta_r^2 \rangle^{1/2} = \begin{cases} F(\alpha)\left(\dfrac{D}{\lambda}\right)^{(\alpha-4)/2}\theta_d^{\alpha-3}, & \alpha < 4, \\[2ex] G(\alpha)\left(\dfrac{r_{sep}}{l_r}\right)^{(\alpha-4)/2}\theta_d, & \alpha > 4. \end{cases} \tag{5}$$

Here r_{sep} is the separation between pierce points through the scattering medium. For a double source (like B2 2050+36) with a component angular separation of θ_{sep}, $r_{sep} = D\theta_{sep}$. The functions $F(\alpha)$ and $G(\alpha)$ are normalization functions that differ from group to group but typically by no more than a factor of a few. For reference, Cordes et al. (1986) predict $\langle \Delta\theta_r^2 \rangle^{1/2} = 0.18$ mas$(D_{kpc}/\lambda_{cm})^{-1/6}\theta_d^{2/3}$ for a Kolmogorov spectrum in a screen located D_{kpc} kpc distant, producing an angular broadening of θ_d mas, and observed at a wavelength of λ_{cm} cm.

In general, if $\alpha > 4$, refractive effects like angular wander dominate over diffractive effects like angular broadening. Thus, one would expect to see the apparent position of a source wander by more than the width of its scattering disk. If $\alpha < 4$, the converse is true.

Table 4 summarizes the 0.61 MHz measurements of the angular separation between the two components of B2 2050+36. We have estimated $\langle \Delta\theta_r^2 \rangle^{1/2}$ using two different methods. Henceforth, we shall also distinguish between the ensemble average expected differential angular wander $\langle \Delta\theta_r^2 \rangle^{1/2}$ and the quantity estimated from the separation measurements $(\bar{\theta}_r^2)^{1/2}$. First, we calculated $(\bar{\theta}_r^2)^{1/2}$ using the standard estimator for the variance and using the three values in Table 4. This estimate is $(\bar{\theta}_r^2)^{1/2} = 2.3$ mas. Second, we estimated $(\bar{\theta}_r^2)^{1/2}$ to be comparable to the maximum

TABLE 4

B2 2050+36 Component Separation Measurements

Epoch	θ_{sep} (mas)	Reference
1984 Aug	60 ± 3	Mutel & Hodges 1986
1988 Jun	56 ± 2	FM93
2000 Jul	56.1 ± 1.0	This work
Differential Angular Wander Upper Limits		
$(\bar{\theta}_r^2)^{1/2}$ (mas)	2.3	
max($\Delta\theta$) (mas)......	4	

difference between component separations at the different epochs max ($\Delta\theta$). This estimate is max ($\Delta\theta$) = 4 mas.

Figure 3 shows $\langle\Delta\theta_r^2\rangle^{1/2}$ as a function of the density spectral index α, as predicted by Cordes et al. (1986), Romani et al. (1986), and Rickett & Coles (1988). We also plot our observational limits $(\bar{\theta}_r^2)^{1/2}$, $3(\bar{\theta}_r^2)^{1/2}$, and max ($\Delta\theta$). In producing Figure 3, we have assumed $D = 2$ kpc. We have considered $\langle\Delta\theta_r^2\rangle^{1/2}$ as a function of both D and α. However, the dependence on D is fairly weak, $\langle\Delta\theta_r^2\rangle^{1/2} \propto D^{-1/6}$ for $\alpha = 11/3$. Reasonable ranges for D produce little difference in $\langle\Delta\theta_r^2\rangle^{1/2}$. The value $D = 2$ kpc is motivated by the distance to the Cygnus superbubble (Bochkarev & Sitnik 1985), through which the line of sight to B2 2050 + 36 passes.

Figure 3 shows clearly that along this line of sight the upper limits on $\langle\Delta\theta_r^2\rangle^{1/2}$ constrain $\alpha < 4$. The largest allowed value, $\alpha = 3.86$, occurs if we adopt an upper limit of $3(\bar{\theta}_r^2)^{1/2}$ and use the expression for $\langle\Delta\theta_r^2\rangle^{1/2}$ from Rickett & Coles (1988). Using a more stringent limit on the differential angular wander max ($\Delta\theta$), the expressions for $\langle\Delta\theta_r^2\rangle^{1/2}$ from Cordes et al. (1986) or Romani et al. (1986), we find $\alpha \lesssim 3.7$. We adopt $\alpha = 11/3$ as a limit based on $(\bar{\theta}_r^2)^{1/2}$ we consider to be overly strict.
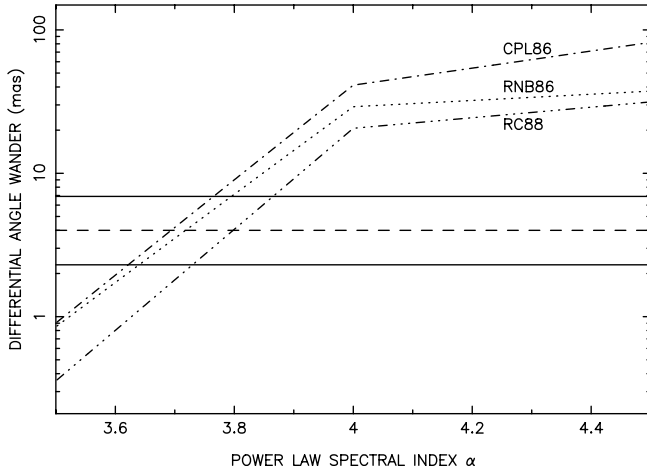

FIG. 3.—Differential angular wander $\langle\Delta\theta_r^2\rangle^{1/2}$ as a function of the density spectral index α. Three expressions for $\langle\Delta\theta_r^2\rangle^{1/2}$ are shown: that of Cordes et al. (1986; *dot-dashed line*), Romani et al. (1986; *dotted line*), and Rickett & Coles (1988; *triple-dot–dashed line*). All expressions are taken from Appendix A of FM93. The abrupt change in slope at $\alpha = 4$ occurs because no attempt has been made to join smoothly the expressions for $\alpha < 4$ and $\alpha > 4$. The solid horizontal lines represent our upper limits on the differential angular wander of B2 2050 + 36 as given by the standard variance estimator of $(\bar{\theta}_r^2)^{1/2}$ and $3(\bar{\theta}_r^2)^{1/2}$. The dashed horizontal line represents our upper limit on the differential angular wander as given by max ($\Delta\theta$).

The standard estimator for the variance, which we have used in determining $(\bar{\theta}_r^2)^{1/2}$, assumes that the measurements are independent. In this case, the independence of the various measurements can be assessed by comparing the interval between the different measurement epochs with the refractive timescale,

$$\Delta t_r = \frac{l_r}{v} = 20 \text{ yr } \frac{D}{2 \text{ kpc}} \left(\frac{v}{10 \text{ km s}^{-1}}\right)^{-1}, \qquad (6)$$

where v is the bulk velocity of the material. FM93 assumed $v = 50$–100 km s^{-1}, for which $\Delta t_r = 2$–4 yr. In this case, all three measurement epochs (Table 4) could be considered independent, although the first two only marginally so. However, if the characteristic velocity of the scattering medium is smaller, by as little as a factor of 2, the refractive timescale would be long enough that the first two epochs (1984 August and 1988 June) could not be considered independent.

If the characteristic velocity is as small as 10 km s^{-1}, then less than one refractive time has elapsed since the first observation, and none of these observations can be considered to be independent. Even if this was the case, we would expect to see some change over the 12 yr time span separating the second and third epochs (1988 June and 2000 July). That essentially no change in the angular separation is seen indicates that max ($\Delta\theta$) provides a reasonably stringent upper limit on $\langle\Delta\theta_r^2\rangle^{1/2}$.

3.2.2. *Refractive Intensity Fluctuations*

In concert with refractive wandering, the large-scale density fluctuations will also produce intensity fluctuations as more or fewer rays are "steered" into the line of sight. In the case of B2 2050 + 36, this will produce independent variations in the flux density of its two components.

FM93 compared the flux densities of the two components between their observations and those of Mutel & Hodges (1986). They found that the flux density of the components was consistent with no change in the 4 yr between 1984 August and 1988 June. Table 5 summarizes these earlier measurements and those reported here.

Because of changes in telescopes, receivers, correlators, and possible intrinsic changes, we do not compare the absolute flux densities of these earlier epochs to our measurements. Rather, we compare the flux density ratio between the two components. As Table 5 shows, the western component has remained at a flux density of approximately 15% that of the eastern component for the past 15 yr.

Goodman & Narayan (1985) present expressions for the rms refractive intensity fluctuation m_r as a function of density spectral index α (see also Rickett 1986). In general, $m_r \sim 10\%$ for $\alpha < 4$ and $m_r \gtrsim 50\%$ for $\alpha > 4$. We determine

TABLE 5

FLUX DENSITY OF B2 2050 + 36 AT 0.61 GHz

Epoch	Eastern (Jy)	Western (Jy)	Ratio	Reference
1984 Aug......	3.8	0.6	0.16	Mutel & Hodges 1986
1988 Jun	3.9 ± 0.1	0.6 ± 0.1	0.15 ± 0.03	FM93
2000 Jul	2.864 ± 0.006	0.374 ± 0.014	0.13 ± 0.01	This work

an observed value $m_r \sim 1.5\%$ from the flux density ratios in Table 5, suggesting $\alpha < 4$. For $\alpha < 4$, the strong scattering, i.e., large SM, determined from the observed scattering diameter (Table 3) means that the rms refractive intensity fluctuation will be only a slowly changing function of α. From our observed value of m_r, we find (eq. [3.1.5] of Goodman & Narayan 1985) $\alpha < 3.85$, consistent with the value found by fitting the angular diameters (Table 3).

3.2.3. Comparison with PSR B2020+28

The pulsar PSR B2020+28 ($8°7$ from B2 2050+36) has been the subject of many monitoring programs designed, at least in part, to measure refractive scattering along the line of sight to it. In all cases, it is found that diffractive scattering dominates refractive scattering, as we find for the line of sight to B2 2050+36.

Smith & Wright (1985) used dynamic spectra obtained at 0.41 MHz to measure the frequency drift rate and estimated that the diffractive scattering angle was at least 5 times that of the refractive scattering angle. Using a structure function analysis of a 0.43 GHz flux density monitoring program, LaBrecque, Rankin, & Cordes (1994) find diffractive scattering to dominate over refractive scattering. Bhat, Gupta, & Rao (1999) monitored the pulsar's flux density at 0.33 MHz and estimated the diffractive and refractive scattering angles toward this pulsar. They found that the diffractive scattering angle was roughly 10 times larger than the refractive scattering angle. They also estimated a density spectrum spectral index of $\alpha = 3.54$. Stinebring & Condon (1990) were unable to observe any refractive modulations of the pulsar's flux density in their multifrequency monitoring program, which is consistent with diffractive scattering dominating on this line of sight.

4. INTRINSIC STRUCTURE AND KINEMATICS OF B2 2050+36

A key assumption in our analysis of the differential image wander is that there is little intrinsic change in the separation of the components. Given that on milliarcsecond scales, many sources show evidence of jets and bulk motion, this assumption clearly must be justified.

We have compared our 1.67 GHz observations with those of Phillips & Mutel (1981). This comparison is somewhat difficult because, in general, different antennas at different locations were used in the two VLBI arrays. Thus, this comparison is necessarily crude, but it will be sufficient to show that our assumption is reasonable.

Phillips & Mutel (1981) cite a separation of 60 mas between the two components from observations in 1979 September. If we fit our 1.67 GHz observations with only two components, we find a separation of 58 mas, *less* than that of Phillips & Mutel (1981). Even allowing for differences in arrays and uncertainties in the fitting, we conclude that any intrinsic change in the separation between the two components is probably less than 1 mas. Over the 20.8 yr separating these measurements, any intrinsic motion is probably less than 0.05 mas yr^{-1}. At a redshift of 0.354 for B2 2050+36 (de Vries et al. 2000) and for an assumed Hubble constant of 65 km s^{-1} Mpc^{-1}, this proper motion corresponds to a projected linear separation velocity of c. Our limit is similar to that found by Shaffer, Kellermann, & Cornwell (1999) for CTD 93, a source with a similar compact double structure.

5. CONCLUSIONS

We have conducted a multifrequency suite of observations on the source B2 2050+36. We have used these observations to confirm and extend previous conclusions, principally those of FM93, regarding interstellar scattering along this line of sight.

Our 0.61 MHz observations form the third epoch of VLBI observations at this frequency. Our observations are separated by 12–16 yr from the previous two epochs. As do previous observations, we find the structure of B2 2050+36 at this frequency to be dominated by two components approximately 56 mas apart. Within the uncertainties of the various measurements, this separation has remained unchanged for the past 16 yr. We can place a reasonably strict limit of 4 mas on any differential image wander caused by refractive interstellar scattering. In turn, this limit implies that the electron density power spectrum along this line of sight has a spectral index near the Kolmogorov value, with a value of 4 being highly unlikely. Since the diffractive scattering diameter of the source at this frequency is 21 mas, we conclude that diffractive scattering dominates along this line of sight.

The most significant source of uncertainty in this limit is probably the velocity at which the scattering material is drifting past the line of sight. A "high" velocity of 100 km s^{-1} would mean that the separations measured at the three epochs are independent. A "low" velocity of 10 km s^{-1} would mean that none of the epochs are independent. Even if the velocity of the scattering material is low, the separation between our observations and the previous ones is probably long enough that, if refractive scattering were important on this line of sight, some change in the apparent separation of the components would be expected. Nonetheless, future observations of B2 2050+36 at 0.61 GHz or similar observations of other sources on lines of sight for which the refractive timescale could be estimated would be useful.

Our observations are in good agreement with a variety of observations on the pulsar PSR B2020+28 (line of sight $8°7$ from B2 2050+36). These observations suggest that diffractive scattering also dominates refractive scattering along the line of sight to the pulsar.

Our quasi-simultaneous observations range from 0.33 to 8.4 GHz. We have used these multifrequency measurements to constrain the frequency dependence of the angular diameter of one component of B2 2050+36. At frequencies below 1 GHz, the structure of the eastern component of B2 2050+36 is dominated by scattering. Fitting for both the density spectrum spectral index α and the scattering diameter θ_d, we find $\alpha = 3.52$ with the value of 4 again highly unlikely. At a nominal frequency of 1 GHz, we find the scattering diameter to be $\theta_d = 7$ mas. We also place a conservative upper limit on the density spectrum inner scale of $l_1 \ll 2000$ km.

We also compared our 1.67 GHz observations to those of Phillips & Mutel (1981), acquired approximately 21 yr previously. We find no evidence for any change in the separation at this frequency. This places a limit on the projected linear separation velocity of the two components of c.

REFERENCES

Armstrong, J. W., Rickett, B. J., & Spangler, S. R. 1995, ApJ, 443, 209
Bhat, N. D. R., Gupta, Y., & Rao, A. P. 1999, ApJ, 514, 249
Bochkarev, N. G., & Sitnik, T. G. 1985, Ap&SS, 108, 237
Clegg, A. W., Fiedler, R. L., & Cordes, J. M. 1993, ApJ, 409, 691
Cordes, J. M., & Lazio, T. J. 1991, ApJ, 376, 123
———. 2001, ApJ, 549, 997
Cordes, J. M., Pidwerbetsky, A., & Lovelace, R. V. E. 1986, ApJ, 310, 737
Cordes, J. M., Ryan, M., Weisberg, J. M., Frail, D. A., & Spangler, S. R. 1991, Nature, 354, 121
de Vries, W. H., O'Dea, C. P., Barthel, P. D., & Thompson, D. J. 2000, A&AS, 143, 181
Desai, K. M., & Fey, A. L. 2001, ApJS, 133, 395
Fey, A. L., & Mutel, R. L. 1993, ApJ, 404, 197 (FM93)
Fey, A. L., Spangler, S. R., & Cordes, J. M. 1991, ApJ, 372, 132
Fey, A. L., Spangler, S. R., & Mutel, R. L. 1989, ApJ, 337, 730
Goodman, J., & Narayan, R. 1985, MNRAS, 214, 519
Gupta, Y., Rickett, B. J., & Lyne, A. G. 1994, MNRAS, 269, 1035
Hewish, A., Wolszczan, A., & Graham, D. A. 1985, MNRAS, 213, 167
Kellermann, K. I., & Owen, F. N. 1988, in Galactic and Extragalactic Radio Astronomy, ed. G. L. Verschuur & K. I. Kellermann (Berlin: Springer), 563
LaBrecque, D. R., Rankin, J. M., & Cordes, J. M. 1994, AJ, 108, 1854

Lazio, T. J., Spangler, S. R., & Cordes, J. M. 1990, ApJ, 363, 515
Molnar, L. A., Mutel, R. L., Reid, M. J., & Johnston, K. J. 1995, ApJ, 438, 708
Mutel, R. L., & Hodges, M. W. 1986, ApJ, 307, 472
Mutel, R. L., Hodges, M. W., & Phillips, R. B. 1985, ApJ, 290, 86
Phillips, R. B., & Mutel, R. L. 1981, ApJ, 244, 19
Rickett, B. J. 1986, ApJ, 307, 564
Rickett, B. J., & Coles, W. A. 1988, in IAU Symp. 129, The Impact of VLBI on Astrophysics and Geophysics, ed. J. Moran & M. Reid (Dordrecht: Kluwer), 287
Rickett, B. J., Lyne, A. G., & Gupta, Y. 1997, MNRAS, 287, 739
Romani, R. W., Narayan, R., & Blandford, R. 1986, MNRAS, 220, 19
Shaffer, D. B., Kellermann, K. I., & Cornwell, T. J. 1999, ApJ, 515, 558
Smith, F. G., & Wright, N. C. 1985, MNRAS, 214, 97
Spangler, S. R., & Cordes, J. M. 1988, ApJ, 332, 346
———. 1998, ApJ, 505, 766
Spangler, S. R., & Gwinn, C. R. 1990, ApJ, 353, L29
Stinebring, D. R., & Condon, J. J. 1990, ApJ, 352, 207
Stinebring, D. R., Faison, M. D., & McKinnon, M. M. 1996, ApJ, 460, 460
Taylor, J. H., & Cordes, J. M. 1993, ApJ, 411, 674
Trotter, A. S., Moran, J. M., & Rodríguez, L. F. 1998, ApJ, 493, 666
Wilkinson, P. N., Narayan, R., & Spencer, R. E. 1994, MNRAS, 269, 67